Unsteady Entropy Measurements in a High-Speed Radial Compressor

M. Mansour
N. Chokani
A. I. Kalfas[1]
R. S. Abhari

LSM, Turbomachinery Laboratory,
Department of Mechanical and Process
Engineering, ETH Zürich,
8092 Zürich, Switzerland

The time-dependent relative entropy field at the impeller exit of a centrifugal compressor is measured. This study is part of a broader effort to develop comprehensive measurement techniques that can be applied in the harsh environment of turbomachines. A miniature unsteady entropy probe (diameter of 1.8 mm) is designed and constructed in the present study. The unsteady entropy probe has two components: a one-sensor fast-response aerodynamic probe and a pair of thin-film gauges. The time-dependent total pressure and total temperature are measured from the fast-response aerodynamic probe and pair of thin-film gauges, respectively. The time-dependent relative entropy derived from these two measurements has a bandwidth of 40 kHz and an uncertainty of ±2 J/kg. The measurements show that for operating Condition A, φ=0.059 and ψ=0.478, the impeller exit flowfield is highly three dimensional. Adjacent to the shroud there are high levels of relative entropy and at the midspan there are low and moderate levels. Independent measurements made with a two-sensor aerodynamic probe show that the high velocity of the flow relative to the casing is responsible for the high relative entropy levels at the shroud. On the other hand, at the midspan, a loss free, jet flow region and a channel wake flow of moderate mixing characterize the flowfield. At both the shroud and midspan, there are strong circumferential variations in the relative entropy. These circumferential variations are much reduced when the centrifugal compressor is operated at operating Condition B, φ=0.0365 and ψ=0.54, near the onset of stall. In this condition, the impeller exit flowfield is less highly skewed; however, the time-averaged relative entropy is higher than at the operating Condition A. The relative entropy measurements with the unsteady entropy probe are thus complementary to other measurements, and more clearly document the losses in the centrifugal compressor. [DOI: 10.1115/1.2799525]

Introduction

A primary goal in the design of turbomachines is to have higher efficiencies and wider operating ranges. Thus, a substantial effort has been made to try and understand the loss mechanisms and their origins in the various components of turbomachines. Although much progress has been made in understanding loss mechanisms, Denton [1], our understanding is still incomplete. The focus of the present work is the structure of the impeller exit flow in a centrifugal compressor. Centrifugal compressors are used in automotive, marine turbocharging and distributed power applications because of their compact design and high stage pressure ratio. At the exit of the centrifugal compressor's impeller, the flow is unsteady, three dimensional, and turbulent. The structure of this complex flowfield is affected by the tip clearance, which in turn affects the compressor efficiency.

The impeller exit flowfield has been examined using various measurement techniques including hot wires, Inoue and Cumpsty [2], pneumatic and fast-response aerodynamic probes, Roduner et al. [3], and laser velocimetery, Strahlecker and Gyarmathy [4], Schleer and Abhari [5]. All measurement techniques have their respective advantages and disadvantages, and thus are complementary. However, it is incontrovertible that only a measurement of entropy can provide a rational measure of loss, Denton [1]. A difficulty, however, is that entropy cannot be measured directly but only inferred from other properties

$$\Delta s = c_p \ln \frac{T}{T_{\text{ref}}} - R \ln \frac{p}{p_{\text{ref}}} \tag{1}$$

This difficulty has limited progress in experimental studies of the loss mechanisms in turbomachines.

The present paper demonstrates the use of a newly designed unsteady entropy probe that is both miniature and robust, and can provide high frequency measurements in the harsh environment of a centrifugal compressor. The measurements made with this new probe provide new insight into the structure of the impeller exit flow. In the next section, the design of the unsteady entropy probe is presented. Then the test facility used for this study is described. A discussion of the measurements then follows. Finally, the paper concludes with a summary and perspective of the ongoing probe development.

Unsteady Entropy Probe

The principal components of the unsteady entropy probe are a fast-response aerodynamic probe (FRAP) and an unsteady total temperature probe, Fig. 1.

The FRAP is a well-established technology in the Turbomachinery Laboratory at the Swiss Federal Institute of Technology Zürich, and thus only a few of its salient details are discussed below. More complete details, including design, construction, and calibration, of the unsteady total temperature probe are presented.

Fast-Response Aerodynamic Probe. The FRAP employs a miniature silicon piezoresistive chip, Fig. 2, that is glued beneath a pressure tap on the probe tip. A constant excitation current I_e is

[1]Current address: Department of Mechanical Engineering, Aristotle University of Tessaloniki, GR-54124 Greece.

Contributed by the International Gas Turbine Institute of ASME for publication in the ASME Journal of Engineering for Gas Turbines and Power. Manuscript received April 27, 2007; final manuscript received August 14, 2007; published online January 22, 2008. Review conducted by Dilip R. Ballal. Paper presented at the ASME Turbo Expo 2007: Land, Sea and Air (GT2007), Montreal, Quebec, Canada, May 14–17, 2007.

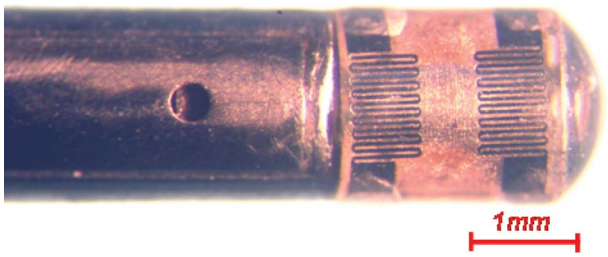

Fig. 1 Photograph of the tip of the unsteady entropy probe

provided to the Wheatstone bridge, which induces an excitation voltage U_e and an output signal voltage U. The output signal is strongly dependent on the pressure differential across the chip and is only weakly dependent on temperature; on the other hand, the excitation voltage is weakly dependent on pressure and more strongly dependent on the temperature. Thus, two-dimensional polynomials, in terms of the excitation and output voltages, are used to yield the sensor calibration relationships for the pressure and temperature. Whereas the frequency response for the pressure is 70 kHz—the limiting factor being the eigenfrequency of the pneumatic cavity that is located between the pressure tap and the diaphragm—an accurate measurement of total temperature is limited to no more than 10 Hz due to the thermal inertia of the chip. More complete details on the FRAP technology are provided by Pfau et al. [6].

Operating Principal: Unsteady Total Temperature Probe. The basic elements of the unsteady total temperature probe are a pair of thin-film gauges that are deposited onto a substrate, Fig. 3, and used as resistance thermometers. The two thin films are mounted azimuthally within an angle of ± 25 deg with respect to the stagnation line, as the Nusselt number is essentially constant over this range [7]. As the heat transfer coefficient α is the same for the two thin films, when the thin-film gauges are electrically heated to two different temperatures T_{f1} and T_{f2},

$$\dot{q}''_{\text{conv1}} = \alpha(T_t - T_{f1})$$

$$\dot{q}''_{\text{conv2}} = \alpha(T_t - T_{f2}) \tag{2}$$

the total temperature of the flow T_t can be determined from

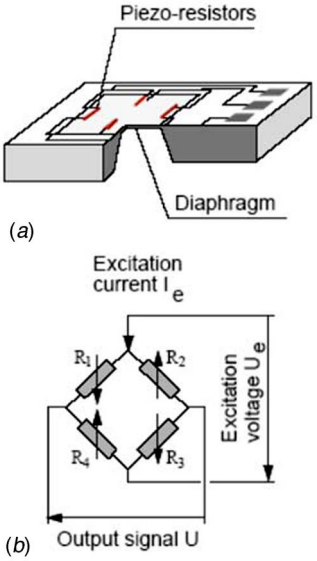

Fig. 2 FRAP: (*a*) miniature silicon piezoresistive pressure sensor chip and (*b*) schematic of Wheatstone bridge

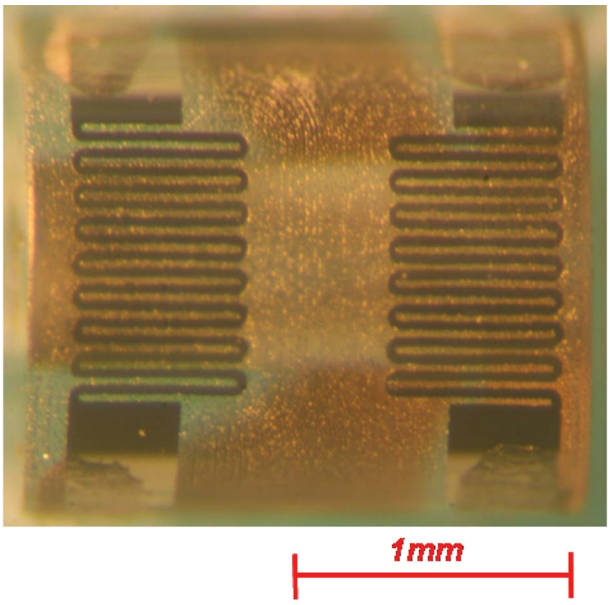

Fig. 3 Unsteady total temperature probe (before integration with the FRAP)

$$T_t = T_{f1} + \frac{\dot{q}''_{\text{conv1}}(T_{f2} - T_{f1})}{\dot{q}''_{\text{conv1}} - \dot{q}''_{\text{conv2}}} \tag{3}$$

This measured temperature is independent of the Reynolds number, Mach number, and the turbulence intensity. Furthermore, the frequency response of the total temperature measurement can be readily made the same as that of the total pressure measured with the FRAP.

The substrate material that is used is fused quartz; its nominal properties are a density of 2203 kg/m^3 and temperature-dependent specific heat and conductivity that are given in Refs. [8,9]. In terms of the thermal and mechanical properties, and adhesive technology, quartz was determined to be the most suitable substrate material. The thin-film gauges are made from 200-nm-thick nickel. In order to assure good adhesion, a 10-nm-thick film of chromium is deposited onto the substrate, prior to sputtering the nickel. As the substrate is a semicylindrical body, the sensor is made by removing nickel using a 20 μm diameter pulsed neodymium-doped yttrium aluminum garnet (Nd:YAG) laser. The resulting serpentine shaped sensor is 30 μm wide and covers a rectangular area of 0.55×0.85 mm^2. Silver leads are deposited at the end of the sensors and run along the flat surface of the semicylinder; then gold wires are wedge bonded to copper wires that are connected to the amplifier.

The diameter of the cylindrical probe is 1.8 mm, and the offset between the thin-film gauges and the pressure sensor is 2.25 mm. Thus although the nondeterministic variation of entropy cannot be measured, by phase locking the deterministic variation in entropy can be quantified.

Calibration: Unsteady Total Temperature Probe. A static calibration, made in an oven, is used to derive the thin-film temperatures of the thin-film gauges that are operated as resistance thermometers. In the calibration, the total temperature probe is exposed to a low speed (5 m/s), isothermal air stream within a channel; the air stream avoids the self-heating of the thin-film gauges and ensures that there is a homogeneous temperature field within the channel. Two thermocouples that are placed in close proximity to the probe are used to measure the temperature of the air stream. The temperature is varied over a range of 20–90°C in steps of 10°C, which corresponds to the temperature range of the present application. The resistances of the thin-film gauges are

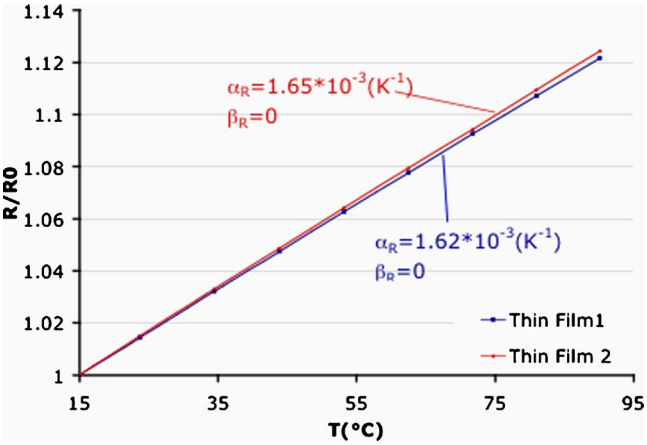

Fig. 4 Static calibration results for unsteady total temperature probe

measured after each increment when thermal equilibrium is achieved. The general form of the temperature-resistance relation is given in Lomas [10]

$$\frac{R}{R_{\text{ref}}} = 1 + \alpha_R(T - T_{\text{ref}}) + \beta_R(T - T_{\text{ref}})^2 \tag{4}$$

Typical calibration results are shown in Fig. 4. It can be seen that the slope is linear for the two thin-film gauges; thus the quadratic coefficient β_R can be neglected. The temperature coefficient of resistance α_R is approximately the same for both thin-film gauges, indicating that the different steps of the manufacturing process are both well controlled and repeatable.

Data Reduction: Unsteady Total Temperature Probe. During the measurements, the thin films are operated at two different constant feeding currents, the Joulean heating of the thin-film gauges is balanced by the conductive and convective heat losses. Thus, the convective heat transfer is given by

$$\dot{q}''_{\text{conv}} = VI - \dot{q}''_{\text{cond}} \tag{5}$$

An electrical circuit is used to pass small constant currents through the thin-film gauges and to measure the corresponding voltages across the thin-film gauges. Thus, the first term on the right-hand side of Eq. (5) is determined from the measured electrical values. On the other hand, the second term on the right-hand side of Eq. (5) is estimated using an unsteady, semi-infinite, heat conduction model; this one-dimensional model is based on the work of Skinner [11], Schultz and Jones [12], Oldfield et al. [13], and Epstein et al. [14]. In this model, the conductive heat transfer rates are solved for using an electrical analog that is composed of a discrete, finite length, series *RC* network. Thus, in terms of the electrical analog, the thermal diffusion equation is written as

$$RC\frac{\partial v}{\partial t} = \frac{\partial^2 v}{\partial x^2} \tag{6}$$

where the voltage v is analogous to temperature T, the capacitance C is analogous to c/ρ, and the resistance R is analogous to $1/k$. The series resistances and capacitances are weighted logarithmically in a manner that is analogous to the logarithmic spacing between nodes that are "placed" across the thermal penetration depth within the substrate. Therefore, an order-of-magnitude fewer series resistances and capacitances can be used to accurately predict the conductive losses than if a linear weighting is used. The discretized set of equations

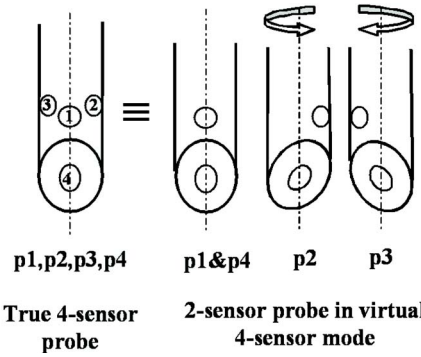

Fig. 5 Measurement concept of a FRAP two sensor in a virtual four-sensor mode

$$\frac{\partial v_i}{\partial t} = \frac{1}{RC}\left[\frac{v_{i-1}}{\Delta x_i \Delta x_{i-1}} - \frac{v_i}{\Delta x_i}\left(\frac{1}{\Delta x_i} + \frac{1}{\Delta x_{i+1}}\right) + \frac{v_{i-1}}{\Delta x_i \Delta x_{i+1}}\right] \tag{7}$$

are solved using a fourth-order, Runge-Kutta method. The boundary conditions for Eq. (6) are derived from the temperatures of the thin-film gauges at the surface and the assumption of a zero heat flux at the depth of thermal penetration. A linear temperature distribution across the thermal penetration depth is assumed in order to provide an initial condition for Eq. (6). The frequency response of the conduction model determines the frequency response of the total temperature measurements, since the electrical circuit has a bandwidth of 120 kHz. The bandwidth of the model used in the present work covers 0.43 Hz–120 kHz with a phase shift of less than 5 deg, which ensures that frequency response of the measured total temperatures is the same as that of the total pressures.

Two-Sensor Fast-Response Aerodynamic Probe

A two-sensor FRAP (2S-FRAP) was used to measure the unsteady velocity field. Pfau et al. [6] describe in detail the use of the virtual four-sensor FRAP, but for sake of completeness brief details are provided below. The 2S-FRAP is calibrated in a virtual four-sensor mode by turning probe into three positions similar to a four-sensor probe, as shown in Fig. 5. A set of four dimensionless calibration coefficients, given in Eq. (8), is determined from this calibration.

$$K_\varphi = \frac{p_2 - p_3}{p_1 - p_m} \quad K_\gamma = \frac{p_1 - p_4}{p_1 - p_m}$$

$$K_t = \frac{p_{\text{tot}} - p_1}{p_1 - p_m} \quad K_s = \frac{p_1 - p_{\text{stat}}}{p_1 - p_m} \tag{8}$$

where $p_m = (p_2 + p_3)/2$. During the measurements, the probe is used in a virtual four-sensor mode. The flow angles are then determined from the yaw (K_φ) and pitch (K_γ) coefficients, and the velocity from the total pressure (K_t) and static pressure (K_s) coefficients. Thus, the three velocity components can be determined.

Error Analysis: Unsteady Total Entropy. Since entropy can only be inferred from other properties, the measurement uncertainty of the entropy probe can only be evaluated in terms of the errors in these other properties. Four properties, the measured total pressure and total temperature, and their respective reference values, are used to determine the entropy, Eq. (1).

The uncertainty in the total pressure is in the range ± 100 Pa, Pfau et al. [6]. The steady total temperature derived from the FRAP has an uncertainty of ± 0.5 K, Kupferschmied [15]. Several sources contribute to the total temperature derived from the unsteady total temperature probe. The propagation error technique is used to combine the uncertainties in these sources into a composite value. The sources (and relative errors) considered here are the output voltage of the constant current electrical circuit (0.1%),

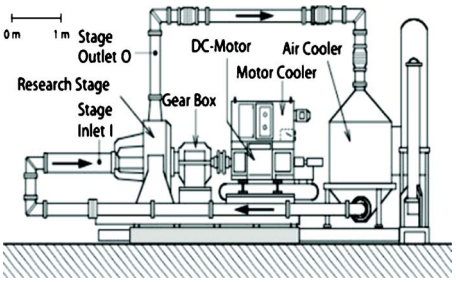

Fig. 6 System layout of the compressor facility "Rigi"

temperature-resistance calibration constants (0.2%), and the materials properties that are used in the conduction model (1.8%). These yield a relative error of 2.5% in the total temperature. The absolute errors on the test rig reference conditions define by Hunziker and Gyrmathy [16] are ±120 Pa for p_{ref} and 0.2 K for T_{ref}.

The relative error in the entropy is expected to be of 2.51%, which is equivalent to an absolute error in the range of ±2 J/kg. This estimated uncertainty is consistent with the reported values for measurements made with the principal components of the unsteady entropy probe.

Test Rig and Measurement Configuration

The test facility is the single stage, centrifugal compressor system, "Rigi," which is located in the Turbomachinery Laboratory. The facility is described in detail in Hunzinker and Gyrmathy [16]. The layout of the system is shown in Fig. 6. It operates in a closed loop with air delivered at a design volume flow rate and a pressure ratio of 3.5 m^3/s and 2.8, respectively.

For the present tests, the system is equipped with a centrifugal impeller followed by a vaneless diffuser. Schleer [17] describes these two components in detail. The impeller is typical of that found in small-scale distributed power generation and automotive turbocharging applications. This scaled-up model matches the main design criteria and nondimensional parameters that are typical of the small-scale devices, and also generates flow structures that are representative of those in small-scale compressors, Schleer et al. [18].

The impeller has seven pairs of full and splitter blades, as shown in Fig. 7. Its outer diameter is 400 mm, and at the impeller exit the blades are swept back by an angle of 30 deg with respect of the radial direction. Immediately downstream of the impeller is

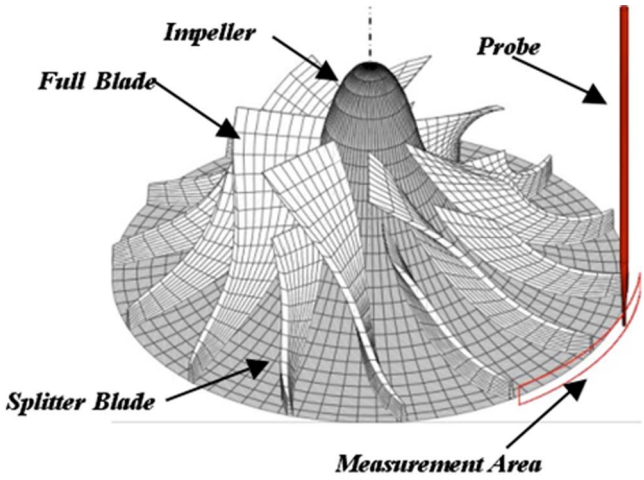

Fig. 7 3D rendering of impeller, showing also location of the unsteady entropy and two-sensor probes and measurement area

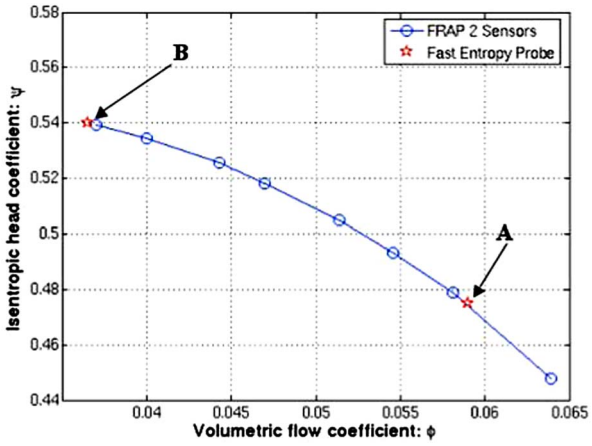

Fig. 8 Operating line for the compressor. A and B are the two conditions at which time-resolved flow measurements are made with the unsteady entropy probe.

a parallel vaneless diffuser with an exit diameter of 580 mm; the diffuser height is 15.7 mm. The clearance ratio, which is defined as the ratio of the tip gap width 0.7 mm and the diffuser height 15.7 mm, is 4.5%. An objective of the present work is to use the newly designed unsteady entropy probe to experimentally quantify details of associated loss generation mechanisms.

The operating line for the compressor at a tip Mach number Ma=0.8 is shown in Fig. 8. The stage inlet reference condition is kept constant to p_{ref}=95,830 Pa and T_{ref}=297 K. Also shown in the plot are the two operating conditions at which unsteady entropy measurements are made. Condition A, φ=0.059 and ψ=0.478, is close to the point of 2 deg flow incidence at the blade's leading edge. Condition B, φ=0.0365 and ψ=0.54, is an operating condition that is close to the onset of stall. The unsteady entropy probe measurements are made at a radial position of R_d/R_{d2}=105% and as illustrated in Fig. 7 are phase locked, using an optical trigger on the shaft, over a full blade passage. A 2S-FRAP is also used to measure the three-dimensional velocity flowfield and flow angularity. Pfau et al. [6] describe the principle of the 2S-FRAP.

The spatial resolution of the measurements using both probes is 0.75 mm in the axial direction, and 0.39 deg azimuthally. At each measurement point, a time series of 400,000 data points is acquired at a sampling rate of 200 kHz using a NI PCI 4452 data acquisition board. All data processing is subsequently done on a laboratory personal computer (PC).

Results and Discussion

As discussed in Ref. [7], the Nusselt number is constant when the thin-film gauges are located on circumferential angles that are within ±25 deg of the stagnation point. Similarly, the calibration of the FRAP is made over a yaw angle range of −30–+30 deg. The circumferentially averaged profiles and phase-locked relative flow angles α_{rel} are shown in Figs. 9 and 10, respectively. The relative flow angle is defined here as the angle between the absolute flow angle (as determined from two-sensor FRAP measurements) and the absolute yaw angle of the unsteady entropy probe. The results in Figs. 9 and 10 show that over the range of application the temperature and pressure measurements are made within the range of validity.

The circumferentially averaged measurements of pressure, temperature, and entropy are presented in Fig. 9 for the two operating conditions. Although the previous laser doppler anemometer (LDA) measurements of Schleer and Abhari [5] show that there are significant flowfield variations in the circumferential direction, the comparison of the circumferentially averaged temperature pro-

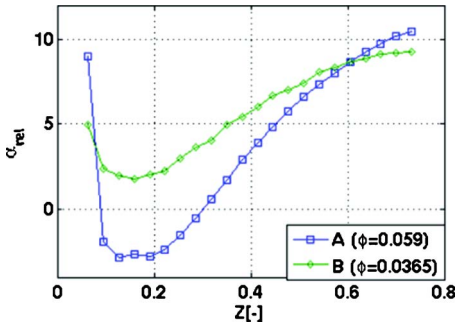

Fig. 9 Circumferentially averaged profiles of relative flow angle α_{rel} at operating Points A (ϕ=0.059) and B (ϕ=0.0365)

files from the piezoresitive chip of the FRAP and thin-film gauges provides one level of assessment of the entropy probe measurements.

As can be seen in Fig. 11, the profiles of the measured temperatures agree very well over the diffuser height. Quantitatively, the differences between the two measurements are no more than 0.8%; this excellent agreement is a validation of the entropy probe's design. Also shown in Fig. 11 is the total pressure distribution that is derived from the FRAP component of the entropy probe. This distribution shows that there are lower total pressures near the shroud wall compared to the hub wall; this suggests that there are more losses in the flow that is adjacent to the shroud. The measured entropy profiles, also shown in Fig. 11, confirm this observation. It should be noted that there are two relative entropy profiles at each operating point, one each derived from the total temperatures measured using the piezoresistive sensor of the FRAP and the thin-film gauges. Both profiles show excellent agreement with each other.

The highly three-dimensional nature of the impeller exit flow is seen in Fig. 12, where the contours of the axial, radial, and tangential velocities are plotted for operating Point A (ϕ=0.059). In

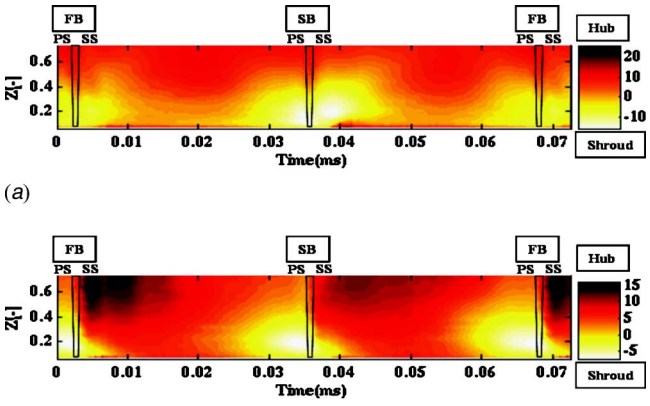

Fig. 10 Time-resolved distribution of relative flow angle α_{rel} (*a*) operating Point A: ϕ=0.059 and (*b*) operating Point B: ϕ=0.0365

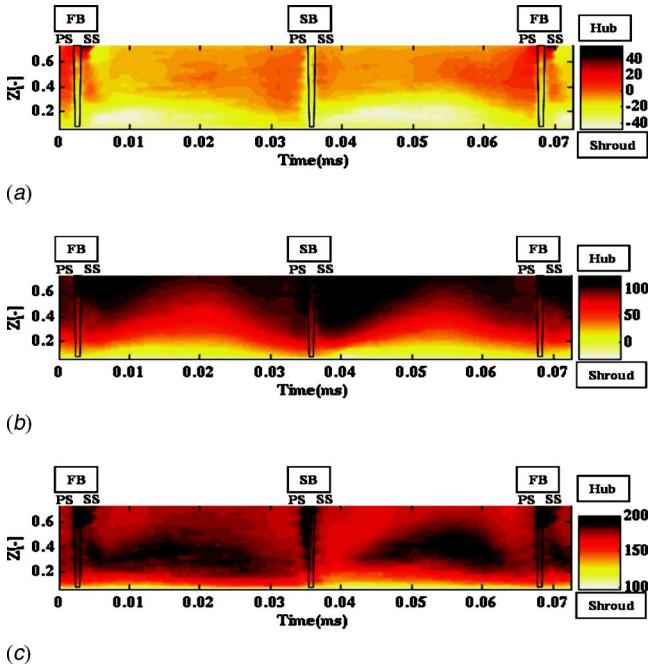

Fig. 12 Time-resolved contours of (*a*) axial velocity, (*b*) radial velocity, and (*c*) tangential velocity, at operating Point A (ϕ=0.059)

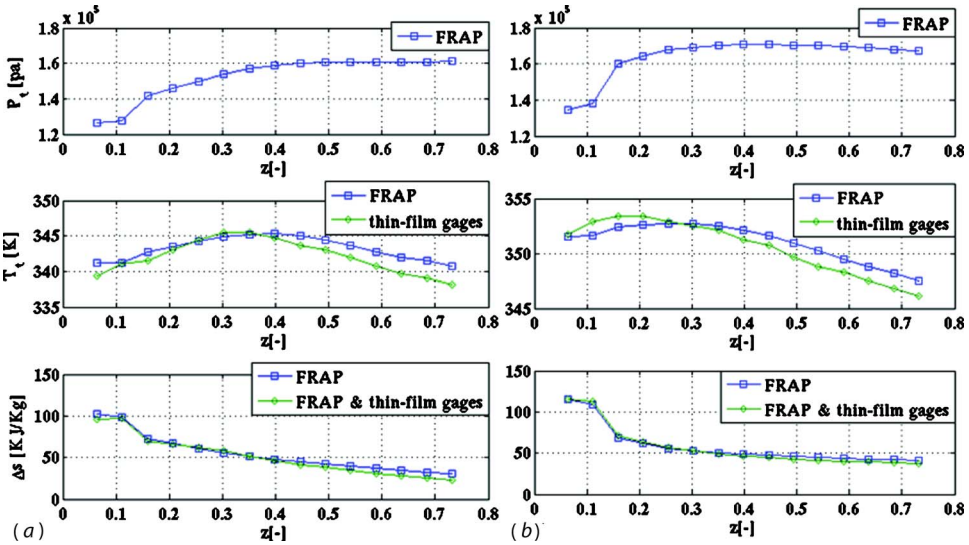

Fig. 11 Circumferentially averaged profiles of total pressure, total temperature, and entropy: (*a*) operating Point A: ϕ=0.059 and (*b*) operating Point B: ϕ=0.0365

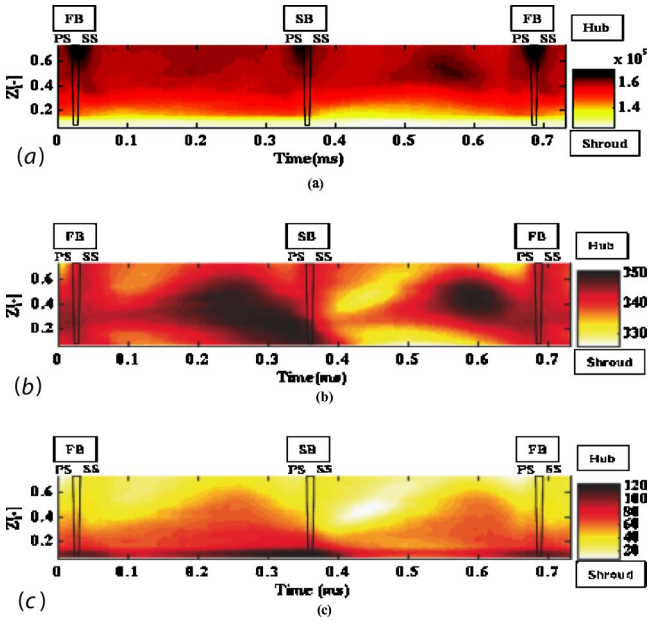

Fig. 13 Time-resolved contours of (*a*) total pressure, (*b*) total temperature, and (*c*) relative entropy, at operating Point A (ϕ =0.059)

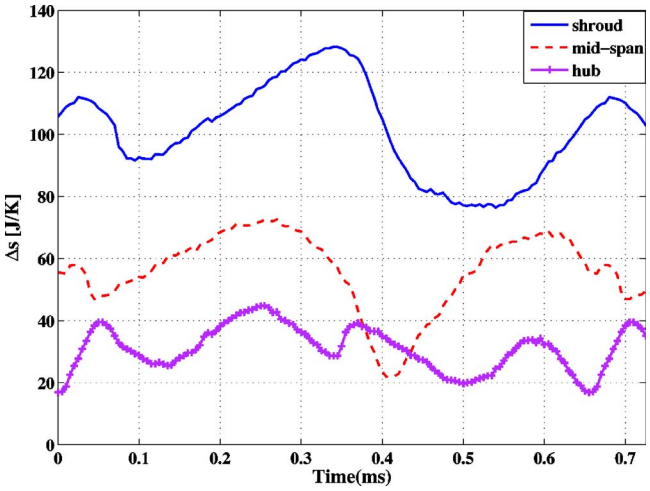

Fig. 14 Circumferential variation of the relative entropy at operating Point A (ϕ=0.059) for three axial positions: *Z*=10% (shroud), *Z*=40% (midspan), and *Z*=70% (hub)

the plots, the blade positions, which are determined from the shaft's encoder signal, are shown. Since the measurements are made downstream of the impeller exit, there is an apparent shift of the flow features relative to the blades. The tangential velocities are relatively high across the height of the diffuser, and relatively low (~100 m/s) tangential velocities are seen only in the near vicinity of the shroud. In this region, adjacent to the shroud, the radial velocities are relatively small in magnitude (±20 m/s) and are alternatively positive and negative along the circumferential direction. The negative radial velocities are seen on the suction side of the blades close to the blade tip, whereas positive velocities are seen on the pressure side. Near the shroud wall, along the blade suction sides, the negative axial velocities are evidence of secondary flows. These secondary flows are more pronounced adjacent to the splitter blade compared to the full blade. Near the hub, the circumferential variation differs from that along the shroud, as relatively high radial velocities occur near the suction side and somewhat smaller radial velocities near the pressure side. Schleer and Abhari [5] have identified this region of high radial and intermediate tangential velocities as a jet flow structure. The intermediate radial velocity/high tangential velocity region that occurs at midspan in the middle of the passage is identified as a channel wake flow. These measurements confirm the highly three-dimensional nature of the impeller's exit flowfield and the profound effect of the tip gap clearance.

The corresponding time-resolved total pressure, total temperature, and relative entropy fields are shown in Fig. 13. The measured total pressures are generally lowered adjacent to the shroud relative to the hub, as suggested by the circumferentially averaged profile shown in Fig. 11(*a*). Figure 13 also shows that there are no strong circumferential variations of the total pressure across the diffuser height. On the other hand, the total temperature field shows that there are gradients both circumferentially and across the diffuser height. The variations are indicative of the skewed nature of the impeller's exit flow. Near the hub on the pressure side of the splitter blade, there is an elongated region of elevated total temperature; on the full blade's pressure side, the region of elevated total temperature is more confined. Skewed regions of relatively low total temperature are seen in the tip clearance region, and this region of low temperature is more pronounced for the splitter blade than for the full blade. These regions of relatively low total temperature are a consequence of upward motion of fluid away from the relative cool shroud wall casing. The heat transfer is especially pronounced in those regions due to the strong secondary flow that is identified in Fig. 12. The contours of the relative entropy field, derived from the total pressure and total temperature measurement, show marked circumferential variations, as a consequence of the total temperature variations. The losses are substantially greater adjacent to the shroud where the high levels of relative entropy are a result of the high velocity of the flow relative to the casing. In the previously identified regions of relatively low total temperature, the levels of relative entropy are not as high due to the effects of the strong secondary flows. These effects are more pronounced at the splitter blade tip. At midspan of the diffuser height, regions of intermediate relative entropy can be seen, and coincide with the channel wake flow that was identified in Fig. 13. On the other hand, the jet flow region has only low level of relative entropy, suggesting that there is little mixing in this region. The circumferential variations of the relative entropy are examined for three axial positions, *Z*=10% (shroud), *Z*=40% (midspan), and *Z*=70% (hub) in Fig. 14. Although the abscissa shows the relative entropy, it is meaningful in this plot to compare the mean and the peak-to-peak variation of three cases. The mean relative entropy increases from the hub toward shroud, as discussed above. It is interesting to note also that while the peak-to-peak range is small (~20 J/kg) at the hub, it is larger and approximately the same (~50 J/kg) at both midspan and shroud positions.

The operating Point B (ϕ=0.0365) that is close to the onset of stall is examined in Figs. 15–17. Similar to the design operating point, examined previously in Fig. 12, the radial velocities in Fig. 15 show that there is a region of reversed flow near the shroud that is caused by the presence of the tip gap.

However, in contrast to the design operating point, the radial velocities in the region between midspan and hub are larger on the pressure side of the blades compared to the velocities on the suction side. Furthermore, the tangential velocities are higher along the suction side compared to the pressure side, which also differs from the design operating point. The classical jet-wake model, first described by Dean and Senoo [19], can be seen in the pattern of radial and tangential velocities.

On the pressure side of the blades, the region of highest radial velocity covers approximately one-third of the passage width and is identified as the jet region. The wake region covers the remaining two-thirds of the passage width, and close to the blades' suc-

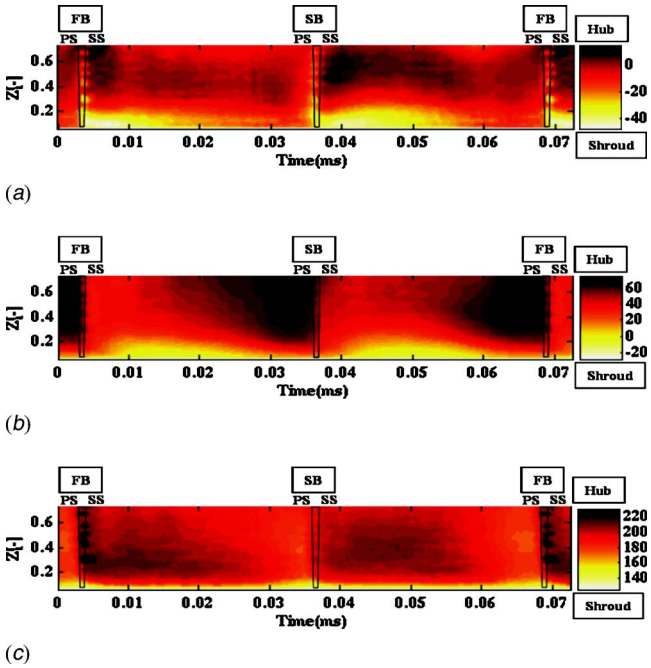

Fig. 15 Time-resolved contours of (*a*) axial velocity, (*b*) radial velocity, and (*c*) tangential velocity, at operating Point B (ϕ =0.0365)

tion side has lower radial velocities and high tangential velocities. The contours of axial velocity show that there are secondary flows along the blades' suction side near the shroud wall. Although the spatial extent of the secondary flow is smaller than that at operating Condition A, shown in Fig. 12, the effect of the flow past the tip of the splitter blade is more pronounced than on the full blade.

Nevertheless, the impeller exit flow is still highly three dimensional, as can be seen from the total temperature field shown in

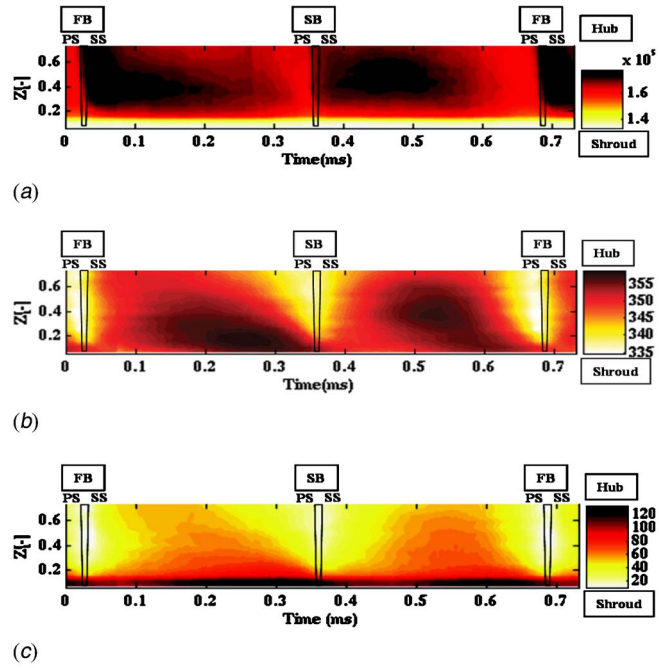

Fig. 16 Time-resolved contours of (*a*) total pressure, (*b*) total temperature, and (*c*) relative entropy, at operating Point B (ϕ =0.0365)

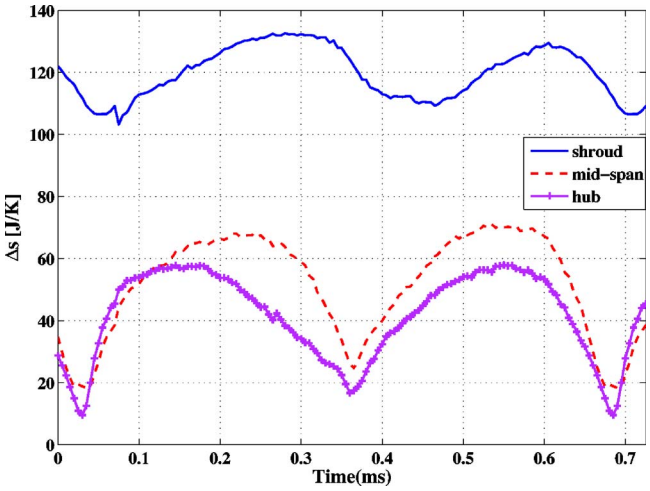

Fig. 17 Circumferential variation of the relative entropy at operating Point B (ϕ=0.0365) for three axial positions: Z=10% (shroud), Z=40% (midspan), and Z=70% (hub)

Fig. 16. Although the flowfield is much less skewed, it is seen that the region of elevated temperature ahead of the full blade is larger compared to that ahead of the splitter blade. The effect of the tip gap on the secondary flow can also be seen in the total temperature distribution. Specifically near the shroud wall there are regions of relatively low total temperature downstream of the blades' suction side. This effect is less pronounced than for operating Point A. In fact, overall, both the total temperature and total pressure flowfields are more uniform for Condition B than those of operating Point A. The time-resolved relative entropy is shown in Fig. 16(*c*). Similar to the design operating point the largest losses occur in the flow that is adjacent to the shroud due to the high flow velocity relative to the casing. The wake region has intermediate levels of relative entropy and the jet region is nearly loss free.

The circumferential distributions of relative entropy at three positions are shown in Fig. 17. It can be seen that the mean values of the relative entropy are similar at the hub and midspan positions. The similar values of relative entropy at midspan and hub confirm that the jet-wake flow spans a large portion of the diffuser height. On the other hand, a higher mean value of the relative entropy is found at the shroud, but the peak to peak fluctuation is less pronounced than for the operating Condition A. This indicates that the tip gap has a smaller effect on the exit flow at the operating Point B. However, the time-averaged relative entropy is 68.2 J/kg, for the Condition B compared to 62 J/kg for the operating condition A. This is due to the fact that the mean values of this relative entropy are in general higher for operating Condition B.

Concluding Remarks

An unsteady entropy probe has been designed, built, and then used to make measurements in a centrifugal compressor. The principal components of the miniature (diameter 1.8 mm) unsteady entropy probe are a FRAP and an unsteady total temperature probe. The FRAP derives total pressure measurements from the electrical output of a miniature silicon piezoresistive chip that is beneath a pressure tap on the probe tip. The total temperature is measured from a pair of thin-film gauges, which are operated as resistance thermometers. An unsteady, semi-infinite, heat conduction model is used to correct the voltages across the thin-film gauges. Thus, high frequency (up to 70 kHz) measurements of the deterministic relative entropy variations of the flow in centrifugal compressor can be made.

The centrifugal compressor is typical of that used in small-scale distributed power generation and automotive turbocharging applications. The impeller has seven pairs of full and splitter blades and is followed immediately downstream by a parallel vaneless diffuser. Phased-locked measurements of the impeller exit flow are made at a fixed radial position. Two operating conditions, one that is near the design point and a second that is close to the onset of stall, are examined. The total pressure, total temperature, and relative entropy measurements of the unsteady entropy probe are complemented with three-dimensional velocities and flow angularity measurements from a 2S-FRAP. At the operating Condition A, the measurements of total pressure and total temperature show that the impeller exit flowfield is highly three dimensional. The total pressures are relatively low at the shroud and relatively high near the hub, on the suction side and pressure side of the blades. On the other hand, the total temperature field is skewed and has gradients both circumferentially and across the diffuser height. Near to the hub on the pressure side of the splitter blade, an elongated region of elevated total temperature is seen and a more confined region of elevated total temperature is seen for the full blade. Therefore, a highly three-dimensional relative entropy field is measured. Adjacent to the shroud high levels of relative entropy are measured, and at the midspan there are regions of low relative entropy interspersed with regions of moderate relative entropy. The independent measurements of the two-sensor aerodynamic probe show that the high velocity of the flow relative to the casing is responsible for the high relative entropy levels at the shroud. On the other hand, at the midspan, the loss free region is associated with a jet flow and the channel wake flow, which has moderate mixing, characterizes the regions of moderate relative entropy. When the centrifugal compressor is operated near the onset of stall, a classical jet-wake model type flow is observed. The wake region, which is close to the blades' suction side, covers approximately two-thirds of the passage width, and has intermediate levels of relative entropy. The jet region, which has the highest radial velocity, is nearly loss free. Similar to the design operating point, the largest relative entropy, and therefore largest losses, occurs in the flow that is adjacent to the shroud; this is due to the high flow velocity relative to the casing. However, although the spatial extent across the diffuser height of the large loss region is smaller at operating Point B than that at operating Condition A, the time-averaged relative entropy is higher for the operating Point B compared to the operating Point A, due to overall higher levels of relative entropy, especially near the hub, where the channel wake flow is still found.

The data from the unsteady entropy probe reveal detailed features of the highly three-dimensional flowfield at the impeller exit of a centrifugal compressor. The steady-state measurements are in very good agreement with the more established FRAP technology. The time-resolved relative entropy measurements are consistent with the velocity component measurements made independently with a 2S-FRAP. The present design of the unsteady entropy probe comprises a single pressure sensor and a pair of thin-film gauges; thus, the velocities must be measured separately from the relative entropy, and analysis is limited to the deterministic fluctuations. A subsequent probe design shall include two pressure sensors with the pair of thin-film gauges; this new design shall enable the simultaneous measurement of the velocity components together with the relative entropy, such that the stochastic fluctuations can be inferred.

Acknowledgment

The authors acknowledge the support of Albert Kammerer in helping to conduct the measurements with the unsteady entropy and 2S-FRAPs. The authors also thank Cornel Reshef for his work in developing the electronic instrumentation and data acquisition system for the unsteady entropy probe, and gratefully acknowledge his continuous support for the development of FRAP and other fast-response measurement techniques at ETH Zürich over the last 20 years.

Nomenclature

c_p = specific heat of the substrate material
D_2 = diameter of impeller tip
FB = full blade
h = enthalpy
I = current
Ma = Mach number at impeller tip $= U_2/\sqrt{\gamma R T_{t,\text{in}}}$
Nu = Nusselt number
p = pressure
PS = pressure side
q = surface heat transfer
Re = Reynolds number
R = gas constant, resistance
Rd = radial position across the impeller
Δs = relative entropy
SB = splitter blade
SS = suction side
t = time
T = temperature
U = voltage signal
U_2 = impeller tip velocity
V, v = voltage
V_0 = inlet velocity
x = distance
Z = axial position measured from shroud to tip

Greek

α = convective heat transfer coefficient
α_R = temperature coefficient of resistance (linear term)
α_{rel} = angle between flow absolute angle and probe zero yaw angle
β_R = temperature coefficient of resistance (quadratic term)
ϕ = specific flow coefficient, $V_0/(D_2^2 U_2)$
ψ = specific work coefficient, $\Delta h_{ts}/U_2^2$

Superscripts

$''$ = per unit of area

Subscripts

2 = impeller outlet
coduction = conduction
convection = convection
$f1, f2$ = thin films 1 and 2
rad = radial
θ = tangential
ref = reference condition
s = static
t = total
x = axial

References

[1] Denton, J. D., 1993, "Loss Mechanisms in Turbomachines," ASME J. Turbomach., **115**, pp. 521–652.
[2] Inoue, M., and Cumpsty, N. A., 1984, "Experimental Study of a Centrifugal Impeller Discharge Flow in a Vaneless and Vaned Diffusers," ASME J. Eng. Gas Turbines Power, **106**, pp. 455–467.
[3] Roduner, C., Köppel, P., Kupferschmied, P., and Gyarmathy, G., 1999, "Comparison of Measurement Data at the Impeller Exit of a Centrifugal Compressor Measured With Both Pneumatic and Fast-Response Probes," ASME J. Turbomach., **121**, pp. 609–618.
[4] Strahlecker, D., and Gyarmathy, G., 1998, "Investigations of Turbulent Flow in a Centrifugal Compressor Vaned Diffuser by 3-Component Laser Velocimetry," ASME Paper No. 98-GT-300.
[5] Schleer, M., and Abhari, R. S., 2006, "Clearance Effects on the Evolution of the Flow in the Vaneless Diffuser of a Centrifugal Compressor at Part Load Condition," ASME Paper No. GT2006–90083.

[6] Pfau, A., Schlienger, J., Kalfas, A. I., and Abhari, R. S., 2003, "Unsteady 3-Dimensional Flow Measurement Using a Miniature Virtual 4 Sensor Fast Response Aerodynamic Probe (FRAP)," ASME Paper No. GT2003–38128.
[7] Schmidt, E., and Werner, K., 1941, "Wärmeabgabe über den Umfang eines Angebblasenen Geheizten Zylinders," Forsch. Ingenieurwes., **12**, pp. 65–73.
[8] Hartunian, R. A., and Varwig, R. I., 1962, "On Thin-Film Heat-Transfer Measurements in Shock Tubes and Shock Tunnels," Phys. Fluids, **5**, pp. 169–174.
[9] 1970, *Thermophysical Properties of Matter*, The TPRC Data Series: Thermal Conductivity Nonmetallic Solids Vol. 2, Y. S. Touloukian and C. Y. Ho, eds., IFI/Plenum, New York; Specific Heat Nonmetallic Solids, Vol. 5.
[10] Lomas, C. G., 1986, *Fundamentals of Hot Wire Anemometry*, Cambridge University Press, London.
[11] Skinner, G. T., 1960, "Analogue Network to Convert Surface Temperature to Heat Flux," American Rocket Society Journal, **30**, pp. 569–570.
[12] Schultz, D. L., and Jones, T. V., 1973, "Heat Transfer Measurements in Short Duration Facility Hypersonic Facilities," Agardograph No. 165.
[13] Oldfield, M. L. G., Burd, H. J., and Doe, N. G., 1982, "Design of Wide Bandwidth Analogue Circuits for Heat Transfer Instrumentation in Transient Wind Tunnels," *16th Symposium of International Center for Heat and Mass Transfer*, Hemisphere, Washington, DC, pp. 233–257.
[14] Epstein, A. H., Guenette, G. R., Norton, R. J. G., and Yuzhang, C., 1986, "High-Frequency Response Heat-Flux Gauge," Rev. Sci. Instrum., **57**, pp. 639–649.
[15] Kupferschmied, P., 1998, Zur Methodik Zeitaufgelöstter Messungen mit Strömungssonden in Verdichtern und Turbinen, Diss ETH No. 12474.
[16] Hunziker, R., and Gyrmathy, G., 1993, "The Operational Stability of a Centrifugal Compressor and Its Dependence on the Characteristics of the Subcomponents," ASME Paper 93-GT-284.
[17] Schleer, M. W., 2006, "Flow Structure and Stability of a Turbocharger Centrifugal Compressor," Diss ETH No. 16605.
[18] Schleer, M., Mokulys, T., and Abhari, R. S., 2003, "Design of a High Pressure-Ratio Centrifugal Compressor for Studying Reynolds Number Effects," *International Conference on Compressors and their Systems*, London, pp. 391–404.
[19] Dean, R. C., and Senoo, Y., 1960, "Rotating Wakes in Vaneless Diffusers," ASME J. Basic Eng., **82**, pp. 563–574.